Trends in cyclones in the high-latitude North Atlantic during 1979-2016

Wickström, S.

2020-01

Wickström , S , Jonassen , M O , Vihma , T & Uotila , P 2020 , ' Trends in cyclones in the high-latitude North Atlantic during 1979-2016 ' , Quarterly Journal of the Royal Meteorological Society , vol. 146 , no. 727 , pp. 762-779 . https://doi.org/10.1002/qj.3707

http://hdl.handle.net/10138/325689
https://doi.org/10.1002/qj.3707

Received: 9 July 2019 | Revised: 11 October 2019 | Accepted: 15 November 2019 | Published on: 25 December 2019

DOI: 10.1002/qj.3707

Quarterly Journal of the Royal Meteorological Society RMetS

RESEARCH ARTICLE

Trends in cyclones in the high-latitude North Atlantic during 1979–2016

S. Wickström[1,2] | M. O. Jonassen[1,2] | T. Vihma[1,3] | P. Uotila[4]

[1]Department of Arctic Geophysics, The University Centre in Svalbard, Longyearbyen, Norway

[2]Geophysical Institute, University of Bergen, Bergen, Norway

[3]Finnish Meteorological Institute, Helsinki, Finland

[4]Institute for Atmospheric and Earth System Research, University of Helsinki, Helsinki, Finland

Correspondence
S. Wickström, Department of Arctic Geophysics, The University Centre in Svalbard PO Box 156, NO-9171 Longyearbyen, Norway.
Email: siiri.wickstrom@unis.no

Funding information
Academy of Finland, 317999

Abstract

We report an increase in winter (DJF) cyclone densities in the areas around Svalbard and in northwestern Barents Sea and a decrease in cyclone densities in southeastern Barents Sea during 1979–2016. Despite high interannual variability, the trends are significant at the 90% confidence level. The changes appear as a result of a shift into a more meridional winter storm track in the high-latitude North Atlantic, associated with a positive trend in the Scandinavian Pattern. A significant decrease in the Brunt–Väisälä frequency east of Svalbard and a significant increase in the Eady Growth Rate north of Svalbard indicate increased baroclinicity, favouring enhanced cyclone activity in these regions. For the first time, we apply composite analysis to explicitly address regional consequences of these wintertime changes in the high-latitude North Atlantic. We find a tendency toward a warmer and more moist atmospheric state in the Barents Sea and over Svalbard with increased cyclone activity around Svalbard.

KEYWORDS

Arctic, Barents Sea, Eady growth rate, extratropical cyclones, Scandinavian pattern, sea ice decline, storm tracks, Svalbard

1 | INTRODUCTION

Extratropical low-pressure systems (hereafter "cyclones") are essential for the energetics of the atmosphere through transporting heat and moisture poleward, which is vital for balancing the net radiative cooling and fresh water deficit in the polar regions (Bengtsson *et al.*, 2006; Sorteberg and Walsh, 2008). Other impacts of cyclones on weather and climate in the Arctic are associated with high winds and precipitation. From an Arctic-wide perspective the cyclone density is highest in the summer (June–August, JJA) (Serreze and Barrett, 2008). However, the cyclone activity, encompassing both the intensity and density of cyclones, in the high-latitude North Atlantic is highest in the winter (December–February, DJF) (Serreze *et al.*, 1993; Zhang *et al.*, 2004) with the highest density found at the northern periphery of the North Atlantic cyclone track; between mainland Norway and Svalbard and further to the east in the Barents and Kara Seas (Simmonds *et al.*, 2008).

The Arctic climate system is transferring into a warmer and wetter state as a result of the unequivocally warming climate (Intergovernmental Panel on Climate Change, 2013; Vihma *et al.*, 2016). The Arctic is warming fastest

in the autumn and winter seasons (Cohen *et al.*, 2014), and the highest warming rates are found around Svalbard and over the Barents Sea (Isaksen *et al.*, 2016; Kohnemann *et al.*, 2017). These areas have, in addition to rapidly rising air temperatures, experienced the highest rates of wintertime sea ice loss (Smedsrud *et al.*, 2010; Onarheim *et al.*, 2015; Onarheim and Årthun, 2017; Lind *et al.*, 2018) in the last few decades. On a more local scale, a decline in sea ice concentration related to increased rates of warm Atlantic water inflow has been observed in the fjords of western Spitsbergen (Cottier *et al.*, 2007; Muckenhuber *et al.*, 2016; Nilsen *et al.*, 2016). Several of the observed changes, both Arctic-wide and locally in Svalbard, have been hypothesized to be associated with climate change-driven large-scale atmospheric circulation changes in this region (Cottier *et al.*, 2007; Nilsen *et al.*, 2008; Isaksen *et al.*, 2016).

Large-scale pressure gradients and related properties (such as latitude, speed and meandering) of the polar-front jet stream drive the position and intensity of the extratropical cyclone tracks transporting heat and moisture poleward (Nakamura *et al.*, 2013; Cohen *et al.*, 2014). Compared to its Pacific counterpart, the North Atlantic storm track typically extends farther into the Arctic, thus making the Atlantic sector the primary gateway of atmospheric heat and moisture into the central Arctic (Tsukernik *et al.*, 2007; Sorteberg and Walsh, 2008; Naakka *et al.*, 2019). In addition to atmospheric heat transport, the oceanic heat mainly enters the central Arctic through the Barents Sea or through the Fram Strait (Aagaard and Greisman, 1975), making this area a hotspot for ocean–atmosphere energy exchange processes. The strength and orientation of the storm track reflect the large-scale state of the atmosphere. The question how large-scale atmospheric flow patterns have and will change in a rapidly warming climate has drawn a lot of attention in recent years (Screen *et al.*, 2018 and references within). Further, as Shepherd (2014) writes, "we have much less confidence in the atmospheric circulation aspects of climate change [compared to the thermodynamic aspect], which are primarily controlled by dynamics and exert a strong control on regional climate". Regarding cyclones being an important component of atmospheric dynamics, several studies have addressed the question of how cyclone activity has changed and will change in the future Arctic (Rinke *et al.*, 2017; Zhang *et al.*, 2004; Sepp and Jaagus, 2011; Li *et al.*, 2014; Koyama *et al.*, 2017; Zahn *et al.*, 2018)

Positive trends in wintertime (DJF) cyclone density in the High Arctic are reported by several studies. Both Rudeva and Simmonds (2015) addressing the period 1979–2013, and Zahn *et al.* (2018) addressing the period 1981–2010, found statistically significant increases (at the 90% level, hereafter "significant") in the cyclone frequency north of the Canadian Arctic, over the Arctic Ocean and around Svalbard during these respective periods. Furthermore, they found a significant decrease in the cyclone frequency over the southern Barents Sea in the winter season. Rudeva and Simmonds (2015) used the ERA-Interim reanalysis (hereafter ERAI), from the European Centre forx Medium-range Weather Forecasts (ECMWF) (Dee *et al.*, 2011) for quantifying these trends. Zahn *et al.* (2018) based their results on four different reanalyses, including the Climate Forecast System Reanalysis (CFSR: Saha *et al.*, 2006) from the National Centers for Environmental Prediction (NCEP), the Japanese 55-year reanalysis (JRA-55: Ebita *et al.*, 2011; Kobayashi *et al.*, 2015) from the Japan Meteorological Agency (JMA), and the Modern Era Retrospective analysis for Research and Applications version 2 (MERRA-2) reanalysis (Gelaro *et al.*, 2017), and ERAI. Zahn *et al.* (2018) report that the different reanalysis products are in good agreement in catching the overall atmospheric circulation patterns, differing, however, to some degree in the magnitude of the trends on a regional level. These differences probably result from the combined effects of differences in model resolution and model physics. Sepp and Jaagus (2011) analysed storm tracks derived from the NCEP/National Center for Atmospheric Research (NCAR) reanalysis dataset from 1948 to 2002, and found a significant increase in the number of cyclones entering the central Arctic. This result was, however, not driven by an increase in the number of cyclones entering from the North Atlantic, but rather from the Pacific sector of the Arctic. However, we note that the NCEP/NCAR reanalysis is the coarsest of the mentioned reanalysis products, with a $2.5° \times 2.5°$ horizontal resolution, and is hence likely less reliable on a regional scale.

The majority of the studies on Arctic cyclones have had primarily the circumpolar perspective with little regional focus. In this study, we focus on the regional changes in cyclone activity in the high-latitude North Atlantic, identified and recognized to be important for both atmospheric and oceanic poleward heat transport as well as climate change, as outlined above. The objectives of this study are (a) to quantify the cyclone climatology and trends (1979–2016) in the high-latitude North Atlantic, (b) to better understand the regional consequences of these trends, and (c) to ascertain the mechanisms possibly responsible for the cyclone climatology changes.

This article is structured as follows: in Section 2 we briefly describe the data, the cyclone tracking algorithm and analysis methods used in this study. Thereafter, in Section 3, we aim to answer the main objectives by presenting and discussing (a) seasonal climatology and trends of cyclone density and cyclone activity within the high-latitude North Atlantic, (b) composite analysis of key climate variables for areas showing significant trends in

winter cyclone density, and (c) trends in climate indices and baroclinicity. In Section 4 we discuss the results in the context of previous studies and conclude the study.

2 | MATERIALS AND METHODS

2.1 | Cyclone tracking

There are a number of different methods for defining and tracking cyclones (Murray and Simmonds, 1991; Hodges, 1995; Serreze, 1995). In our study we utilize the Melbourne University cyclone tracking scheme (Murray and Simmonds, 1991), which is shown to perform well in a number of comparison studies (Neu *et al.*, 2013; Simmonds and Rudeva, 2014). This cyclone tracking scheme builds upon scanning a given mean sea-level pressure (MSLP) field and comparing the Laplacian of the pressure field between adjacent grid points. After identifying a pressure depression, an iterative approximation to the centre of the ellipsoid of best fit to the MSLP field is used to locate the low-pressure centre. A physical interpretation of the Laplacian of the pressure field is that it can be seen as a measure of the cyclone intensity (Petterssen, 1956). In the Melbourne University tracking scheme, the threshold for the average value of the Laplacian is set to 0.2 hPa·(° latitude)$^{-2}$ by default over a radius of 2° for depressions to be recognized as cyclones. In this study, however, we focus only on strong cyclones that have an average value of the Laplacian above 0.7 hPa·(° latitude)$^{-2}$ with a defined centre (closed). Also, to avoid erroneous results due to extrapolation of MSLP over regions with high orography, we neglect data from the regions above 1,000 m above sea level (ASL) that is, mainly Greenland in our domain of interest. We also filter out cyclones with lifetimes shorter than 48 h (8 track points). In this work we track explicitly extratropical cyclones in the high latitudes and these should not be confused with polar lows.

Several studies have proved the high quality of ERAI (Dee *et al.*, 2011) in the Arctic (Dufour *et al.*, 2016; Koyama *et al.*, 2017; Naakka *et al.*, 2018), and we therefore chose to use the MSLP fields from ERAI (at the native horizontal grid resolution of 0.75°× 0.75°) for the cyclone tracking. We ran the cyclone tracking algorithm for the time period from 1979 to 2016, with a 6 h output interval.

2.2 | Analysis of track data

For the cyclone track statistics, we binned the cyclone track points geographically in boxes of 400 km × 400 km (indicated in the map in Figure 2a). Given the typical horizontal length and velocity scales of synoptic-scale cyclones, we found this bin size to be appropriate without compromising on the horizontal resolution.

We refer to the number of cyclone track points per season within each of the geographical bins as the "cyclone density". Furthermore, following Zhang *et al.* (2004) we use a cyclone activity index (CAI) to integrate information on cyclone intensity, frequency, and duration in each geographical bin. For a given season and geographical bin, this index is defined as the cyclone density times the mean cyclone intensity;

$$CAI = cyclone\ density \times cyclone\ intensity, \qquad (1)$$

where the intensity is defined as the Laplacian of the pressure field (Petterssen, 1957). The mean cyclone intensity refers to the mean of the intensities of the cyclones in a given box at a given time.

We used the non-parametric Theil–Sen slope estimator (Theil, 1949; Sen, 1968; Eqn (9) in Yilmaz and Perera, 2015) for calculating the magnitude of the linear trends in both cyclone density and cyclone activity.

2.3 | Statistical significance

In order to quantify the statistical significance of the temporal trends in cyclone density, we have used the well-established Mann–Kendall type *t*-test (Mann, 1945; Kendall, 1975). The Mann–Kendall test is a non-parametric test, which means that no assumption is made about the sample size nor about a normal distribution. Also, being a rank-based test the Mann–Kendall test is less sensitive to outliers, relative to parametric tests. The exact equations used in our work can be found as Eqns (1)–(4) in Yilmaz and Perera (2015).

Furthermore, we used Monte-Carlo simulations to assess the significance of anomalies between the climatology and composites of the different climate variables. These simulations are done by picking out random time series, with the same length as the composite, from the seasonal climatology. In our study this procedure was repeated 1,000 times to produce a synthetic probability distribution. The original composite is considered statistically significant if it is at the 90th percentile of this probability distribution. As it turns out, the mentioned anomalies are statistically significant virtually everywhere and we therefore decided not to indicate this significance in the presentation of the corresponding results in Section 3.

2.4 | Composite analysis

To gain an understanding of the regional impacts of cyclone activity, we calculate composites for the nine key climate variables: MSLP, 2 m air temperature, turbulent

fluxes (latent + sensible heat fluxes), long-wave radiation (decomposed into upwelling and downwelling), Z500 − Z1000 geopotential layer thickness, precipitation and vertically integrated divergence of dry static ("thermal" in ERAI) and latent-heat energy fluxes. The latter energy flux is derived from the corresponding moisture flux field in ERAI.

The composites of each field are defined as the mean of the field (daily resolution) for cases with cyclone activity in the regions of interest (defined in Figure 1). The difference between the seasonal mean field of these variables and the composites is the anomaly.

2.5 | Eady growth rate

We calculate the 500 hPa Eady growth rate (Eady, 1949), as is done by for example, Koyama *et al.* (2017):

$$EGR = 0.31 * \frac{f\, d\boldsymbol{v}}{N\, dz}. \tag{2}$$

Here f is the Coriolis parameter, N is the Brunt–Väisälä frequency, $d\boldsymbol{v}/dz$ is the vertical wind shear, $\boldsymbol{v}$ is the horizontal wind vector and z is the height of the atmospheric layer of interest. Following Simmonds and Lim (2009) and Koyama *et al.* (2017) we use the atmospheric layer encompassed by the 300 and 700 hPa pressure levels. The vertical wind shear $d\boldsymbol{v}/dz$ is related to the horizontal temperature gradient via the thermal wind equation (Wallace and Hobbs, 2006). The Brunt–Väisälä frequency is a measure of atmospheric static stability given by:

$$N = \sqrt{\frac{g}{\theta}\frac{d\theta}{dz}}. \tag{3}$$

Here g is the gravitational acceleration, θ is the potential temperature, and $d\theta/dz$ is the vertical gradient of potential temperature. We use the 300, 500 and 700 hPa pressure-level potential temperatures in calculating N at each grid point. Hence, the Eady growth rate depends on both the static stability and horizontal temperature gradients in the atmosphere.

The zonal and meridional winds, air temperature, and geopotential height fields are taken directly from the ERAI reanalysis and the potential temperature field is calculated utilizing the temperature and pressure fields from ERAI. As recommended by Lim and Simmonds (2009), daily averages are used for the Eady growth rate calculations.

3 | RESULTS

3.1 | Seasonal changes in cyclone activity

Figure 1 presents a map of our study region, encompassing the area 60°W to 70°E and 64°N to 90°N. The region was chosen to capture extratropical cyclone activity over the North Atlantic and all the way to the Central Arctic, through the Fram Strait and via the Barents Sea.

In the high-latitude North Atlantic, we observe the highest cyclone densities in the Fram Strait and southern Barents Sea in all seasons except summer (Figure 2a,e,i,m). The average seasonal cyclone density in these regions is up to 16 cyclone track points in a 400 × 400 km domain during a 3-month season, translating to over five cyclone track points per month. This is a result of the North Atlantic storm track splitting in two distinct branches as it approaches Svalbard from the southwest. Especially in the winter (DJF) and autumn (September–November, SON) seasons a high cyclone density band reaching from Iceland into the Arctic is evident (Figure 2; location names in Figure 1), than in the Fram Strait and Barents Seas (Figure 2i). This is in agreement with Serreze and Barrett (2008), who also found high cyclone densities in the summer for the Central Arctic. However, whereas they found these to be the highest cyclone densities for any season and region, we find the highest densities in the Central Arctic in SON. However, we note that our study region only covers the parts of the Central Arctic located within 60°W and 70°E.

As expected, the seasonal geographical patterns in CAI (Figure 2c,g,k,o) follow closely the geographical patterns in cyclone density (Figure 2a,e,i,m), however, with some differences between the seasons. The cyclone densities in the Barents Sea and the Fram Strait are rather similar in SON, DJF and March–May (MAM), while DJF generally has the highest CAI for these areas. This is because the DJF cyclones are on average more intense than the MAM and SON cyclones. This agrees well with several previous studies documenting the North Atlantic storm track activity being highest in the winter (Zhang *et al.*, 2004). Furthermore, we see that the difference between the JJA CAI and the CAI in the rest of the seasons is even more pronounced than the differences between the seasonal cyclone density fields. This indicates that the cyclones, in addition to being fewer in summer in the Fram Strait and the Barents Sea, are also weaker (have lower intensity) compared to the other seasons.

Considering trends in cyclone densities over the period 1979 to 2016, we see the strongest ones in DJF (Figure 2b), which is in line with previous studies (Rudeva and Simmonds, 2015; Zahn *et al.*, 2018). In the Fram Strait, Greenland Sea and Barents Sea regions, we find the strongest positive trends around Svalbard. These are +1.3 cyclone track points per decade west of Svalbard (hereafter Region A) and +3 cyclone track points east of Svalbard (hereafter Region B). The strongest negative trends of −4.5 cyclone track points per decade are located in the southern Barents Sea (hereafter Region C). The Regions A, B and C are

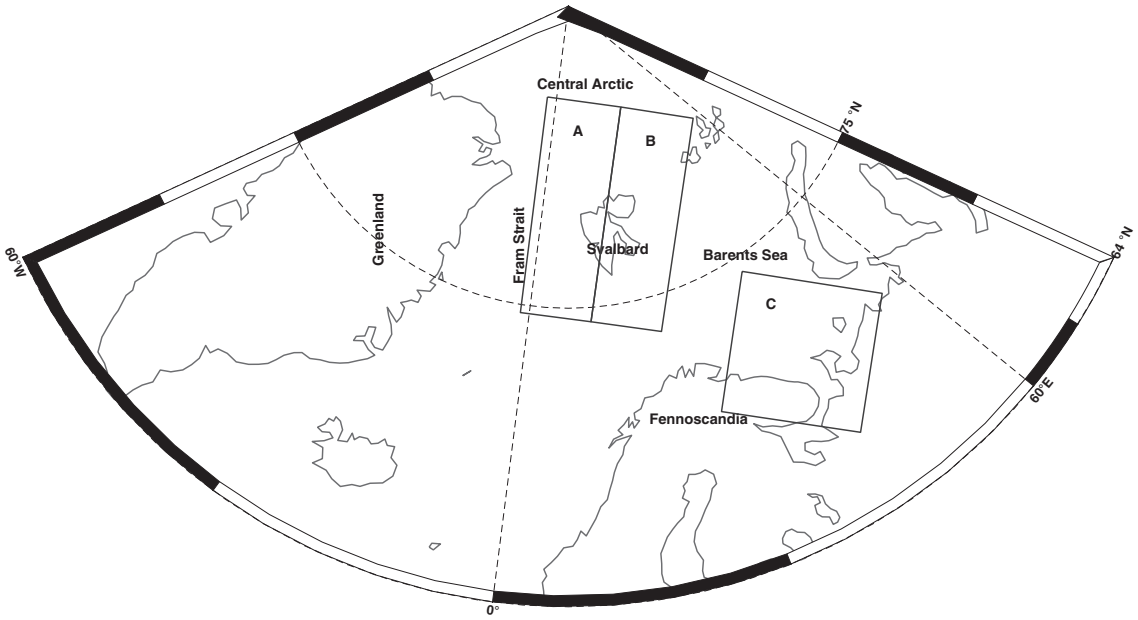

FIGURE 1 Map showing the domain of interest in this study and labels on relevant oceans and air masses

marked in Figure 1, along with the names of geographic regions. The positive trends in cyclone density are significant in all individual patches in Region B and in half of the patches in Region C (Figure 2b).

Considering temporal variability in DJF cyclone densities across the regions A, B and C on an annual level (Figure 3), we see that Regions A and C have average annual densities in the range between 5 and 25 cyclone track points (Figure 3a,c), with the total cyclone track point count for the whole period being 1,487 and 1,950 respectively. The corresponding range for Region B is from 1 to 22 cyclone track points, with a total of 1,194 track points (Figure 3b). The generally lower cyclone densities in region B compared to Regions A and C can be explained by the climatological positions of the DJF North Atlantic storm track branches over the Fram Strait and the southern Barents Sea (Figure 3a). All regions show a large interannual variability as expected with the turbulent nature of extratropical cyclones. Furthermore, we see that all of these regions have significant trends at the 90% confidence level when all parts of the regions are considered (Region A: $p = .082$, Region B: $p = .08$ and Region C: $p = .009$).

Returning to trends in cyclone densities for the other seasons, spatially almost similar, but generally weaker trends in cyclone density, compared to DJF, are found in SON (Figure 2n). MAM trends (Figure 2f) are similar to those in winter in the western Barents Sea and east of Svalbard (around Region B), but opposite in the Fram Strait (Region A, a weak decrease in cyclone density) and in the southern Barents Sea (Region C, insignificant increase). The JJA trends are rather different from the other seasons; there is a significant negative trend in cyclone density northwest of Svalbard (northern parts of Region A) and a significant positive trend just east of Region B and in parts of Region C (Figure 2j).

CAI (Figure 2d,h,p) shows similar spatial patterns to the trends in cyclone density for all four seasons, but fewer geographic bins have statistically significant values. The difference between significance in the trend fields of cyclone density and CAI coincides with cyclone intensity trends (not shown) being insignificant for this period.

As described above, the strongest trends in both cyclone density and CAI, in the high-latitude North Atlantic, are found in DJF. In addition, together with SON, DJF is the season where the strongest near-surface warming rates are found (Cohen *et al.*, 2014). Hence, to limit the scope of this study, we hereafter only focus on the DJF season.

3.2 | Composite analysis

A central aim of this study is to better understand the regional-scale consequences of changes in DJF cyclone activity. To this end, we have calculated the difference between the seasonal mean and the composite of events with a cyclone centre in each region (Regions A, B and C) to produce anomalies for the following fields: MSLP, 2 m air temperature, turbulent fluxes, long-wave radiation, Z500 − Z1000 layer thickness, precipitation and vertically integrated divergence of latent and dry static energy fluxes, as described in Section 2.3. The number of cases used in

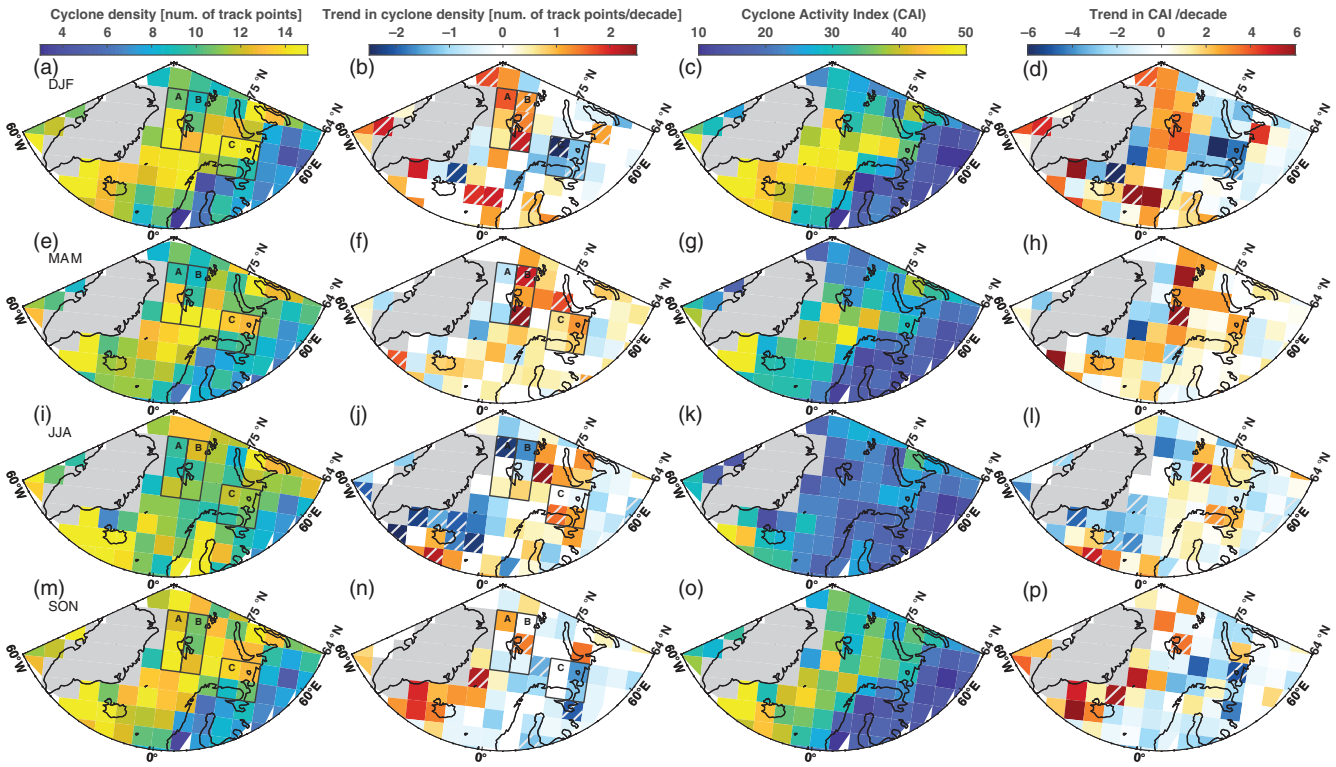

FIGURE 2 (a–p) Seasonal (rows) climatology and trends of cyclone density (number of track points in a given grid box per season) (columns 1 and 2) and cyclone activity index (CAI) (columns 3 and 4) for the period 1979–2016. The grid shows the 400 × 400 km geographical bins used for the cyclone track data. The hatching marks the bins with a significant trend (90% level). Greenland is filtered out due to high elevations. The boxes labelled A, B and C are the areas we have identified as hot spots of DJF change in cyclone density

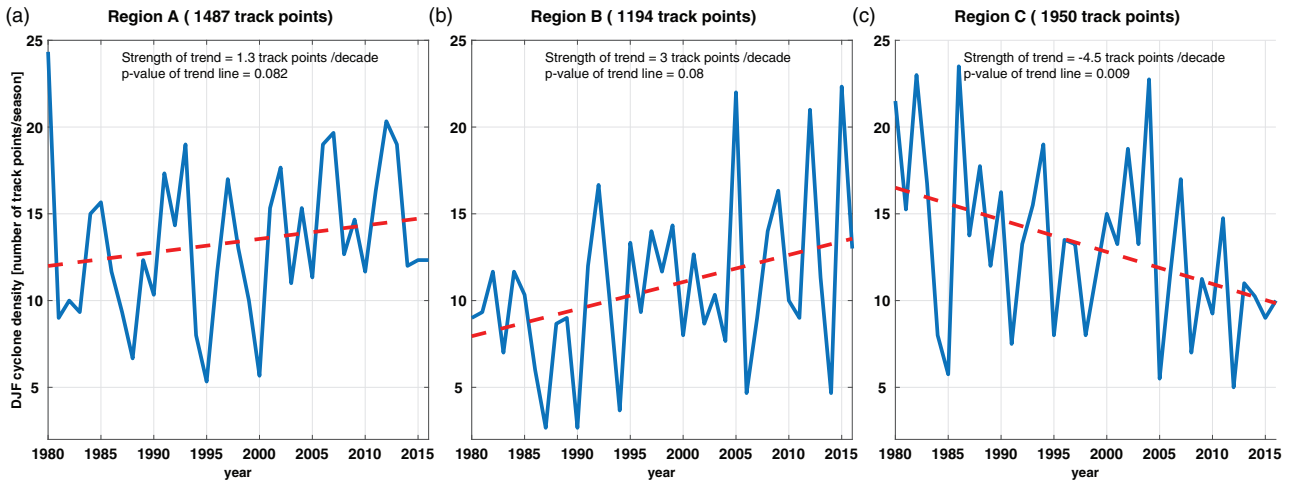

FIGURE 3 Time series of DJF cyclone density and the linear trend in the period 1979–2016 in (a) the Fram Strait (region A), (b) East Svalbard (region B) and (c) the southern Barents Sea (region C). The title indicates how many DJF cyclone track points were located in these regions during the study period

calculating the anomalies for each region is indicated in Figure 3.

The climatological mean fields of MSLP, 2 m air temperature, and daily precipitation are shown in Figure 4a–c respectively. MSLP anomalies of events with a cyclone in Region A (Figure 4d), west of Svalbard, show 5 hPa lower than climatology MSLP values in the Fram Strait and up to 8 hPa higher pressure over most of Fennoscandia. The 2 m air temperatures are slightly above their climatological values (1–2 K) along the North Atlantic storm track. As would

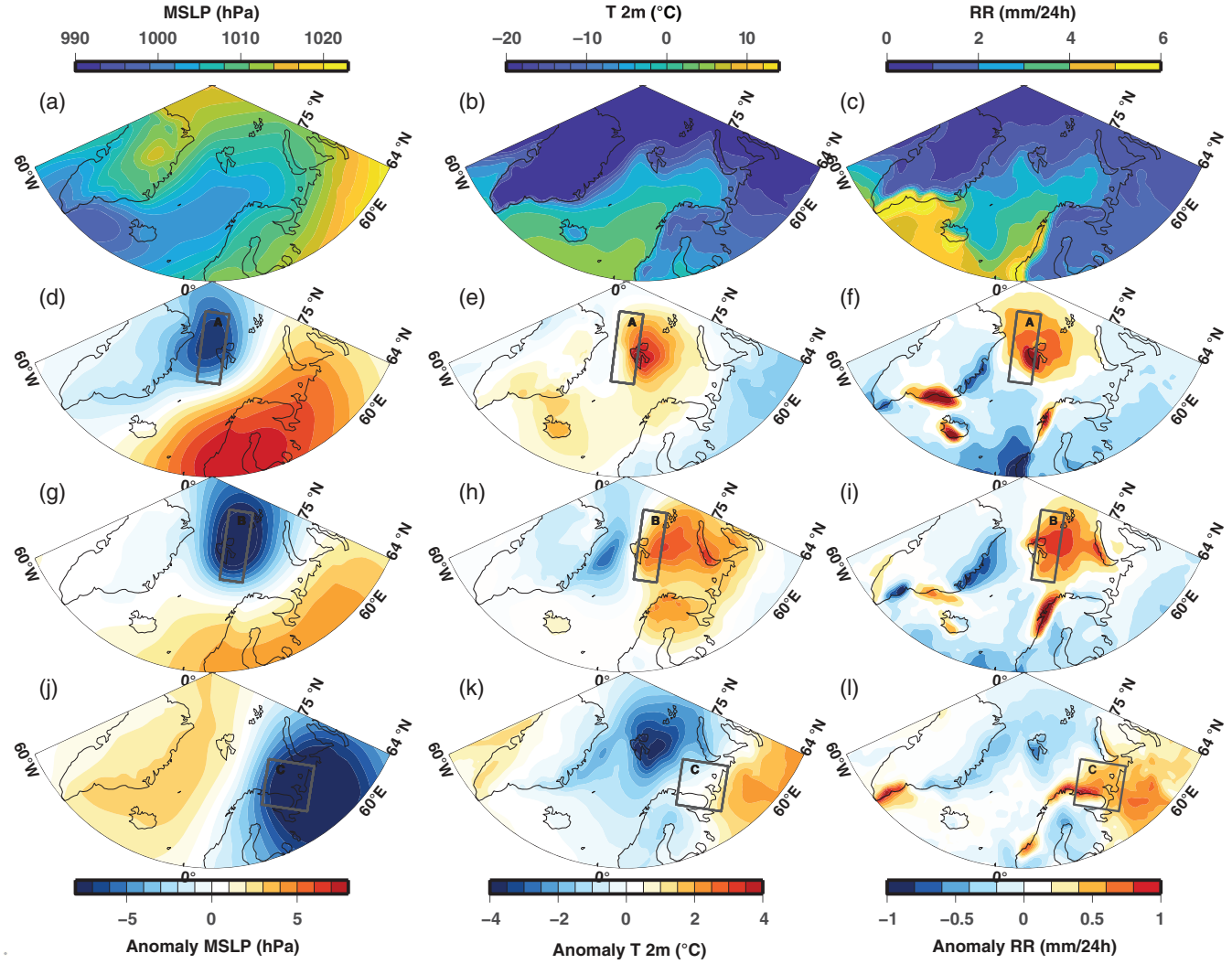

FIGURE 4 DJF climatology of (a) mean sea-level pressure (MSLP), (b) 2 m air temperature (T), (c) precipitation (RR), and composites from these when a cyclone centre is in (d–f) region A, (g–i) region B and (j–l) region C. The sign convention is such that all fluxes are defined positive (negative) toward (away from) the surface

be expected in a warm sector of an extratropical cyclone, the strongest positive anomaly (up to 4 K) is located over Svalbard and extends to the north and east (Figure 4e). These events are also associated with a positive precipitation anomaly, which has the highest values (up to 1 mm per 24 h) for about the same region as the strongest positive temperature anomaly (Figure 4f). The alignment of the strongest positive precipitation and temperature anomalies agree well with the warm sector and the associated frontal precipitation in an extratropical cyclone.

Compared to MSLP anomalies for Region A, the anomalies for Region B are shifted eastward with the lowest surface pressure in the western Barents Sea (Figure 4g). Also, the negative MSLP anomaly for Region B is stronger (−8 hPa), and the positive anomaly over Fennoscandia and northwestern Russia is weaker (4 hPa). The difference in the negative MSLP anomalies between composites for Regions A and B is probably a consequence of Region A being closer to the Fram Strait branch of the North Atlantic storm track than Region B. In line with the pressure anomaly, the 2 m air temperature anomalies are also shifted eastward, with anomalously warm (up to 4 K above climatology) temperatures over most of the Barents Sea and northern Scandinavia and cold (down to −2 K below climatology) over the Fram Strait (Figure 4), when compared to composites for Region A. The cyclonic flow, deduced from the pressure (anomaly) patterns, centred on Region B sets up a flow pattern with warm-air advection over the Barents Sea and cold-air advection over the Fram Strait. As expected in a warm sector of an extratropical cyclone (Bjerknes, 1919), a positive precipitation anomaly of up 1 mm per day aligns well with the warm temperature anomaly over the Barents Sea (Figure 4i).

During the events with a cyclone in Region C (southern Barents Sea), the MSLP field is characterized by a positive anomaly of up to 3 hPa along the east coast of

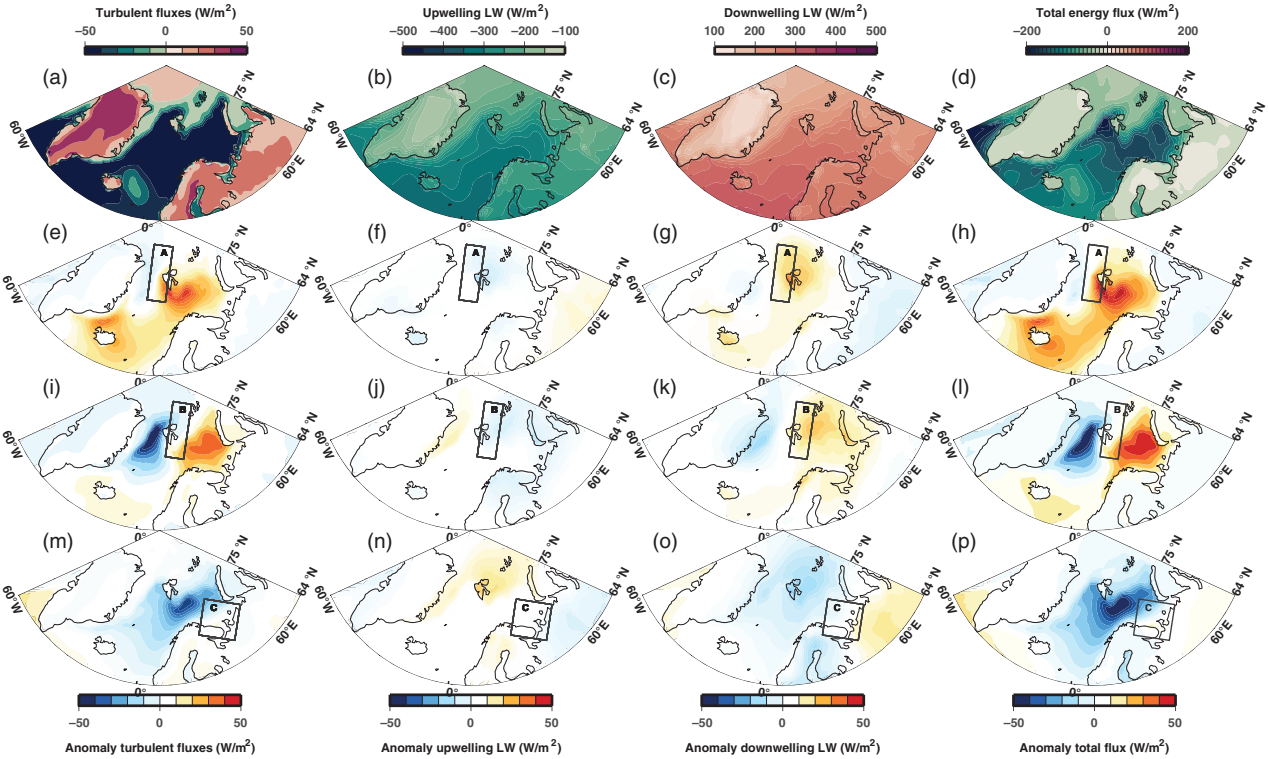

FIGURE 5 Four DJF climatologies of (a) turbulent fluxes (latent and sensible), (b) surface to atmosphere long-wave (thermal) radiation (defined negative), (c) atmosphere to surface long-wave (thermal) radiation (defined positive), (d) total flux (sum of (a), (b) and (c)), and composites from these when a cyclone centre is in (e–h) region A, (i–l) region B and (m–p) region C. The sign convention is such that all fluxes are defined positive (negative) toward (away from) the surface

Greenland, setting up a northerly flow through the Fram Strait together with the negative anomaly over the southern Barents Sea reaching into northwestern Russia and Fennoscandia (Figure 4j). The resulting cold-air advection over Svalbard is accompanied by a negative 2 m air temperature anomaly, reaching −4 K in region B (Figure 4k). These events are also associated with a positive precipitation anomaly of up to 1 mm per 24 h over the northern coast of Fennoscandia and southeastern Barents Sea, leaving the rest of the high-latitude North Atlantic drier than the climatology (Figure 4l). This precipitation anomaly again follows the temperature anomaly. However, the intensification of the anomaly at the coast is most likely orographic enhancement of precipitation.

Anomalies of surface fluxes of turbulent heat and long-wave radiation are a key for understanding the regional consequences of changes in DJF cyclone density on the surface energy balance. We define the fluxes from the point of view of the surface, where positive (negative) fluxes are directed toward (away from) the surface. The high-latitude North Atlantic experiences polar night most of DJF and, hence, solar short-wave radiation is neglected in this study.

The climatological sea ice extent is seen in the DJF climatological turbulent energy flux fields (Figure 5a), with generally a turbulent energy gain over land masses and sea ice and a loss over the open sea. A transition zone of slightly negative turbulent fluxes (−10 to 0 $W \cdot m^{-2}$) between the open water and the positive fluxes in the Central Arctic marks the marginal ice zone. In these regions, the DJF thermal long-wave radiative balance contributes to the net surface cooling, with the seasonal average of the upwelling component (Figure 5b) dominating over the downwelling component (Figure 5c).

The events with a cyclone centre in Region A are associated with a positive turbulent flux anomaly (less heat loss) up to 40 $W \cdot m^{-2}$ covering the southwestern parts of the Barents Sea and reaching to the west coast of Svalbard (Figure 5d). Given the climatological turbulent heat loss of similar magnitudes in these regions (Figure 5a), the net turbulent flux approaches zero or the sign of the flux reverses, turning the atmosphere into a weak turbulent heat source during these events. In the western Fram Strait there is a weak negative (stronger surface heat loss) turbulent flux anomaly down to −10 $W \cdot m^{-2}$, corresponding to a cold-air outbreak regime in that region, set up by the northerly wind field advecting cold and dry Arctic air masses over relatively warm open water.

The composites for the events with a cyclone centre in Region A show an increase in both the upwelling

(the negative anomaly in Figure 5e) and downwelling long-wave radiation (positive anomaly in Figure 5f) around Svalbard. The downwelling radiation anomaly is positive in a band from Iceland into the Barents Sea, indicating an active North Atlantic storm track with associated frontal clouds. A thick frontal cloud, typically associated with extratropical cyclones, is one of the most efficient processes in raising surface temperatures in the Arctic in the dark season (Vihma and Pirazzini, 2005). The upwelling long-wave radiation has a negative anomaly above Svalbard reaching into the Central Arctic and the northern Barents Sea. No strong anomaly is seen to the southwest, contrary to the downwelling radiation. There is a geographic mismatch between anomalies in upwelling and downwelling long-wave radiative components (Figure 5e,f) over the open ocean. Even though the upper ocean receives more heat when cyclones are in Region A, its impact on the surface temperature and, hence, on upwelling long-wave radiation remains minor because the heat received via downwelling long-wave radiation is mixed in the ocean surface layer with a large heat capacity.

With a cyclone in region B, a positive anomaly of $40\,\mathrm{W{\cdot}m^{-2}}$ covers most of southeastern Barents Sea and a corresponding negative anomaly of $-40\,\mathrm{W{\cdot}m^{-2}}$ is centred on the Fram Strait. These anomalies are well in agreement with the northerly wind field set up on the western side of the cyclone centre located in Region B, advecting cold air masses from the Central Arctic over the relatively warm ocean in the Fram Strait and the south-southwesterly flow bringing warm air over the Barents Sea on the eastern side of the cyclone. The upwelling long-wave radiative flux is a function of the surface temperature and, thus, the region in the northern Barents Sea with the strongest positive 2 m air temperature anomaly also has a negative outgoing long-wave radiative flux anomaly (more surface heat loss, Figure 5h). However, the anomalously high downwelling long-wave radiative flux driven by increased cloudiness in the warmer and more moist air masses exceeds that of the upwelling anomaly so that the anomaly of net long-wave radiation anomaly heats the surface (about $20\,\mathrm{W{\cdot}m^{-2}}$) in Region B. The long-wave radiative anomalies have opposite signs in the western Fram Strait. Cold air advection and possible sea ice export in the East Greenland Current might account for the positive outgoing long-wave radiative anomaly (less than climatology surface heat loss), matching with a cold surface anomaly (Figure 4h).

The cold-air outbreak in the Fram Strait, driven by the flow field associated with a cyclone in Region B, with strong turbulent surface heat loss (Figure 5g), drives atmospheric convection. A positive anomaly in upwelling long-wave radiation (i.e. less long-wave radiation emitted by the surface) is present in the ice-covered western Fram Strait (Figure 5h), where the snow/ice surface temperature rapidly responds to cold air. On the contrary, no anomaly is present in the open parts of the Fram Strait, because the sea-surface temperature is not sensitive to a synoptic-scale cold-air outbreak.

Cyclone activity in Region C, in contrast to Regions A and B, is characterized by large turbulent surface heat loss that is up to $40\,\mathrm{W{\cdot}m^{-2}}$ stronger than the climatology southeast of Svalbard. In line with Figure 4b,k, the upward long-wave radiation has a positive anomaly over sea ice (Figure 5k) as the surface is losing less heat in these conditions due to the colder surface temperatures. Similarly, the downward long-wave radiation is anomalously low both in the Fram Strait and the Barents Sea in line with the relatively cold and dry air masses.

Finally, we consider the total energy flux (Figure 5d,h,l,p), which we have calculated as the sum of the turbulent and long-wave radiation energy fluxes. We see from the average of the entire time period (Figure 5d) that in sum the fluxes considered contribute generally to a net heat loss at the surface in the study area during DJF. Furthermore, it is clear that the turbulent surface energy fluxes dominate over the long-wave energy fluxes in forming the total energy flux anomalies connected to cyclones in Regions A, B and C (Figure 5h,l,p). Also, we note that the areas most strongly affected by these anomalies are the Barents Sea with surroundings waters and large parts of the Fram Strait.

Moving up from the surface layer; to gain an understanding of regional consequences in the free atmosphere, driven by cyclonic activity, the final part of the composite analysis focuses on anomalies in the Z500 − Z1000 layer thickness and vertical integrals of heat transport divergence. The climatological distribution of the geopotential layer thickness (Z500-Z1000) is close to zonal with a southward gradient (Figure 6a). The layer thickness is an indirect measure of the air-mass temperature in the mid- to low troposphere. Hence, the zero line in the Z500-Z1000 anomalies can be interpreted as the mean position of the baroclinic zone, with the given cyclone centre location. For both Regions A and B (Figure 6d,g) the Z500-Z1000 anomaly fields display air masses warmer (thicker) than climatology air masses over Fennoscandia and the Barents Sea (positive Z500-Z1000 anomalies of up to 50 m) and colder than climatology over the Fram Strait, which is in line with the above-discussed northerly wind field west of the cyclone centre. The positive Z500-Z1000 anomaly with relatively warm air masses reaches further north into the northern Barents Sea with cyclones in Region A, compared to Region B. Region A has also a more meridionally oriented baroclinic zone between the positive and negative anomalies running over Svalbard (Figure 6d,g). Region B has the baroclinic zone more zonally south of Svalbard. In these events the air masses over Svalbard are

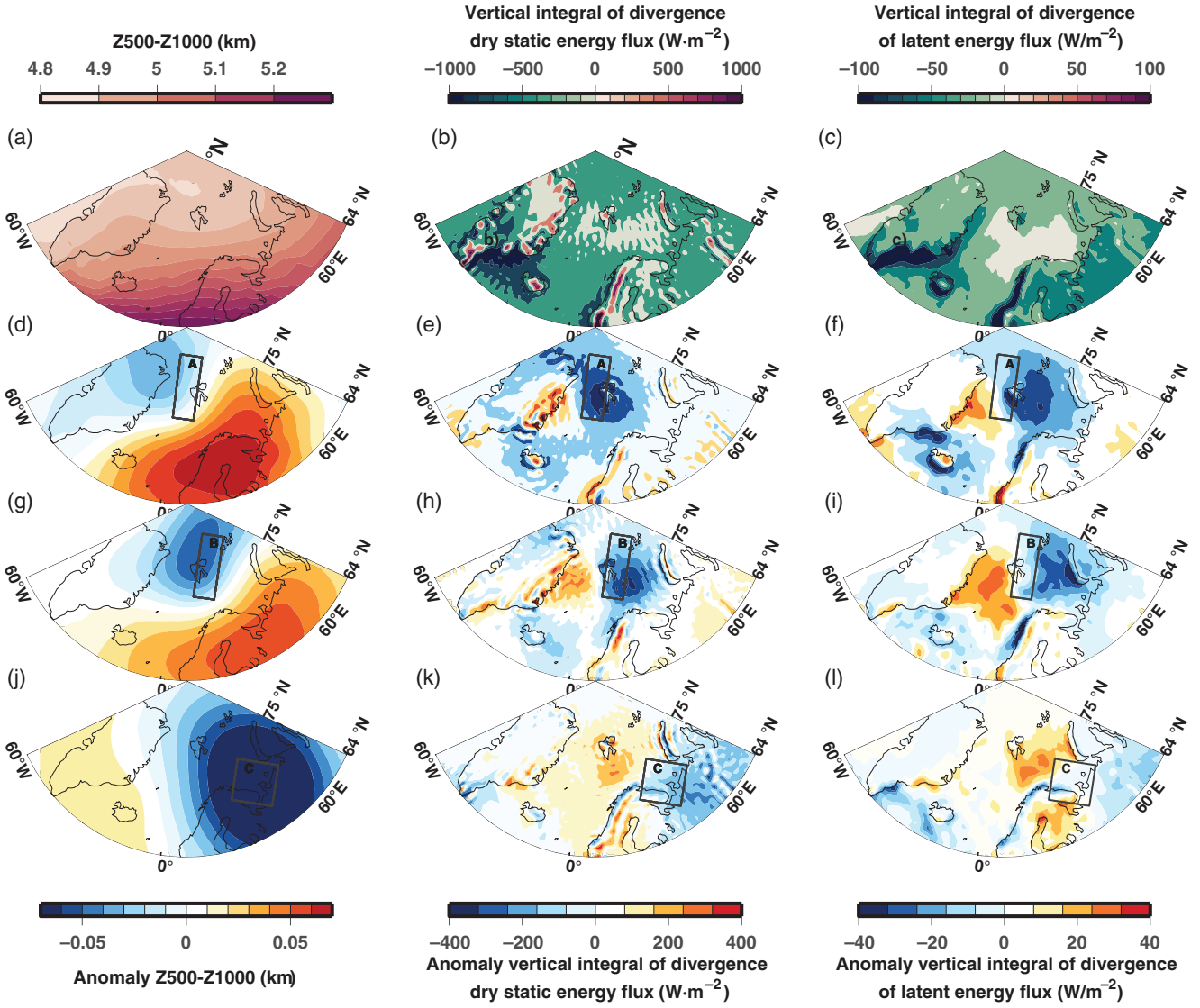

FIGURE 6 DJF climatology of (a) Z500 − Z1000, (b) vertical integral of divergence of dry static energy transport, (c) vertical integral of divergence of latent-heat transport, and the composites of their anomalies when a cyclone centre is in (d–f) region A, (g–i) region B and (j–l) region C

colder than the climatology. The negative anomaly, down to −50 m, for Region B (Figure 6g) is centred over the Fram Strait, being stronger than the corresponding anomaly for Region A (Figure 6d) with a −30 m anomaly centred over northeastern Greenland. The anomalies for Region C show a vast negative Z500-Z1000 thickness anomaly, down to −50 m, covering Svalbard, the Barents Sea, Fennoscandia and northwestern Russia (Figure 6j), suggesting that the air masses flowing around the cyclone centre are of Arctic origin.

To better understand the energetics related to the trends in cyclone activity, we here consider in the following anomalies of vertical divergence of the transport of latent heat and dry static energy over the full atmospheric column (Figure 6, columns 2 and 3). We note that the average DJF dry static energy transport convergence is an order of magnitude larger than that of the latent heat (Figure 6b,c). In line with the net atmospheric poleward transport of energy, convergence dominates over the northern North Atlantic for both dry static energy and latent heat, the DJF mean being close to zero or slightly negative in Regions B and C (Figure 6c).

For cyclone centres in the Fram Strait (Region A), both the dry static energy and latent-heat transport divergence have negative anomalies over and around Svalbard (Figure 6e,f), indicating above-climatology heating in the region. The anomalies in the divergence in the dry static energy transport are larger than those of the latent heat. Region B has similar bimodality as Region A, with dry static energy and moisture transport convergence east of the Svalbard archipelago and divergence in the Fram Strait. This bimodal distribution aligns well with

TABLE 1 DJF trends in climate variables over the period 1979–2016 (change per decade)

	Region A	Region B	Region C
2 m air temperature (°C)	Trend: 1.1 °C/decade ($p < .001$)	Trend: 0.69 °C/decade ($p < .001$)	Trend: 0.58 °C/decade ($p < .001$)
Upwelling long-wave radiation ($W{\cdot}m^2$)	Trend: 3.9 $W{\cdot}m^2$ /decade ($p < .001$)	Trend: 2.6 $W{\cdot}m^2$ /decade ($p < .001$)	Trend: 2.1 $W{\cdot}m^2$/decade ($p < .001$)
Downwelling long-wave radiation ($W{\cdot}m^2$)	Trend: 4.2 $W{\cdot}m^2$ /decade ($p < .001$)	Trend: 2.6 $W{\cdot}m^2$ /decade ($p < .001$)	Trend: 3.2 $W{\cdot}m^2$/decade ($p < .001$)
Z500 − Z1000 layer thickness (km)	Trend: 0.01 km/decade ($p = .02$)	Trend: 0.01 km/decade ($p = .09$)	Trend: 0.01 km/decade ($p = .000$)

Note: The regions A, B and C are indicated on the map in Figure 2a.

the synoptic situation with cold-air advection west and warm-air advection east of the cyclone centre. In Region C, the divergence fields have a positive anomaly indicating larger-than-climatological cooling effect, in line with advection of cold and dry air over the region in cases with cyclones in Region C.

To summarize the local impacts of DJF cyclone activity: with cyclone activity in Regions A and B, the Greenland Sea and Barents Sea regions experience warmer and wetter winter conditions (Figure 4e,h,f,i), whereas with cyclone activity in Region C, the composites are colder and drier than the DJF climatology in regions A and B (Figure 4k). The MSLP field associated with composites of Regions A and B indicate a northerly wind in the Fram Strait, west of the cyclone centre, advecting cold air into Regions A and B with a compensating southerly wind to the east of the centre (Figure 4d,g). This is seen as an anomalous surface heat loss (gain) in the regions with cold (warm) advection in both the turbulent flux and long-wave radiative fields (Figure 5e–p). Region C is again showing generally colder and drier conditions over Svalbard, with a net surface heat loss in most of the Barents Sea (Figures 4k,l and 5p).

Further, we have calculated the trends in the climate variables (Table 1). At a 95% significance level we find a warming trend in all regions of interest (Region A: 1.1 °C/decade, Region B: 0.67 °C/decade and Region C: 0.58 °C/decade). Also, both upwelling and downwelling long-wave radiation have significant positive trends reflecting surface warming and increase in the cloudiness and water vapour in the atmosphere. In line with the general warming, the Z500-Z1000 layer thickness has a positive trend of 10 m/decade. The trend in the Z500-Z1000 layer thickness is, however, significant only in Region A. MSLP, precipitation intensity, turbulent fluxes and the vertically integrated divergent fluxes of dry static energy and latent heat do not have significant trends in the regions of interest.

3.3 | Trends in cyclone densities and their relation to climate indices

We have so far shown that the cyclone densities have significant temporal trends around Svalbard (Regions A and B) and in the southeastern Barents Sea (Region C), and our composite analysis suggests that the consequences of these changes are warmer and wetter winter conditions around Svalbard (Figures 4–6). We now move on to the third, and last objective of the study; connecting the documented cyclone density trends to larger-scale climate indices and, in Section 3.4, to baroclinicity.

The temporal and spatial variability in cyclone tracks is related to the variability in the surface pressure field, and, thus, to climate indices (typically derived from empirical orthogonal functions of the MSLP field) characterizing such variability. We here correlate three well-established climate indices encompassing the North Atlantic: the Scandinavian pattern (SCA), the Arctic Oscillation (AO) and the North Atlantic Oscillation (NAO) with the DJF cyclone densities. The indices were downloaded from the National Weather Service Climate Prediction Center (https://www.cpc.ncep.noaa.gov/data). Positive phases of AO and NAO indicate a zonal polar tropospheric jet stream (Barnston and Livezey, 1987). Opposite to AO and NAO, the positive phase of the SCA (Barnston and Livezey, 1987) represents a large-scale atmospheric state with a high-pressure ridge, typically a blocking high, over the Scandinavian peninsula. This pattern favours a meridional storm track, steering cyclones into the Fram Strait rather than into the southern Barents Sea and northern Scandinavia (Bueh and Nakamura, 2007; Vihma *et al.*, 2019).

The results from our correlation analysis (Figure 7) show that for SCA the correlations are predominantly negative in the region from Iceland to the Barents Sea and positive in the Fram Strait. Hence, the correlation pattern of SCA and cyclone density is roughly the opposite of that

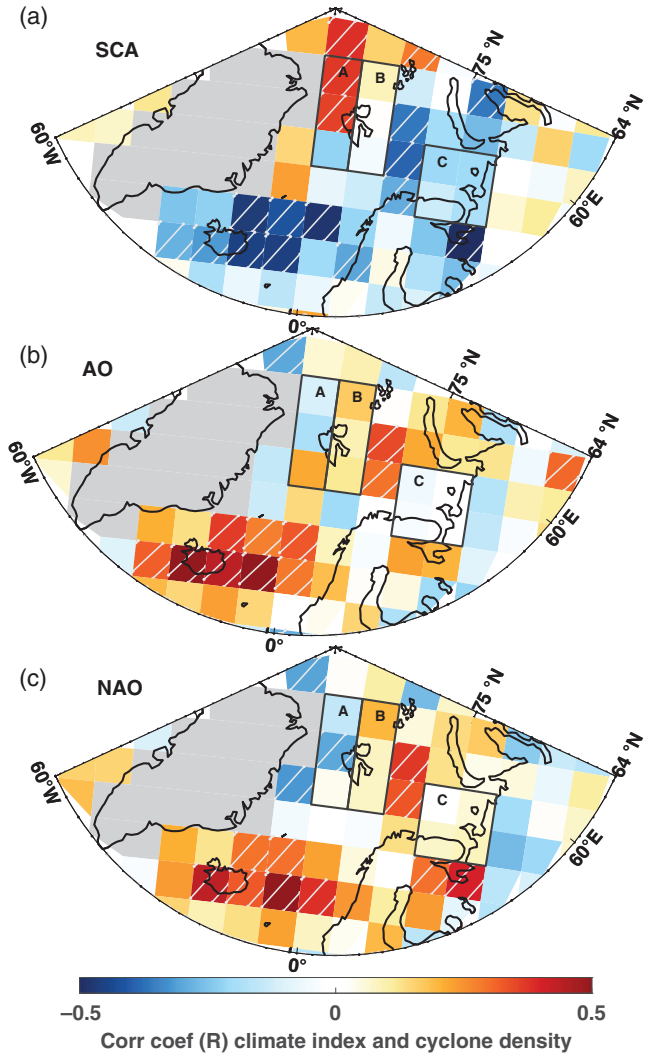

FIGURE 7 Correlation between DJF cyclone densities (number of track points) and (a) the Scandinavian pattern, (b) the Arctic Oscillation and (c) the North Atlantic Oscillation. The boxes labelled A, B and C are the areas we have identified as hot spots of DJF change in cyclone density. Areas where the trends are significant (90% level) are hatched

of AO and NAO (Figure 7b,c), which display negative correlations in larger parts of the Fram Strait and positive correlations around Iceland and the central Barents Sea. NAO can be considered a local (Atlantic) component of AO and it is not surprising that these indices have similar correlation patterns with cyclone density in the study region.

Amongst the climate indices, SCA generally displays the strongest correlations with the cyclone densities for Regions A, B and C. The trend in SCA over the time period of interest is positive (trend = 0.013/year, $p = .16$). Furthermore, there are significant positive correlations between SCA and cyclone density within Region A and significant negative correlations in the vicinity (west) of Region C. Thus, the positive trend in SCA, though not statistically significant, supports to some degree the documented positive (Regions A and B) and negative (Region C) trends in cyclone densities.

3.4 | Changes in baroclinicity

Baroclinicity is a key driver for intensification and persistence of extratropical cyclones.

Central parameters in this regard are N and EGR, the latter of which is a measure of baroclinic instability at the mid-tropospheric level and, thus, a measure of the potential for cyclones to develop and grow (see Equation 2 in Section 2). N is the buoyancy frequency (see Equation 3 in Section 2), which is incorporated in EGR together with the vertical wind shear, accounting for the buoyant fraction of the available potential energy for cyclone intensification and persistence in the given layer. Both parameters have been applied several times in previous studies to assess changes in extratropical cyclones (Simmonds and Lim, 2009; Koyama *et al.*, 2017).

The DJF climatology of N (Figure 8a) shows, as expected, a positive meridional gradient (increasing with increasing latitude). At 64°N, N is around 0.0105 s^{-1} and at 90°N it is around 0.013 s^{-1}. We find a negative trend in the DJF N in the Greenland Sea and the Barents Sea regions in the period 1979–2016 (Figure 8c). This trend likely reflects the observed winter warming in these regions, which is strongest close to the surface (Cohen *et al.*, 2014). The negative trend in N is significant ($p < .1$, hatched areas in Figure 8c) in most parts of Region B and in one patch in Region C.

The DJF climatology of EGR (Figure 8b) shows a northward decreasing potential for cyclone growth, which is in agreement with the northward increasing static stability (Figure 6a), as EGR is an inverse function of N. In DJF, EGR has a significant positive trend north of Svalbard (3×10^{-3} day^{-1}) reaching to the North Pole (Figure 8d). This is a region with climatologically high static stability and low EGR in winter (Figure 8a,b). Further, in addition to N, EGR is a function of the mid-tropospheric wind shear, which is often dominated by the strength of the tropospheric jet stream. In the high-latitude North Atlantic region, the Arctic front jet stream is the most likely source of wind shear. Since the statistically significant changes in N mostly do not align with the statistically significant changes in EGR, we attribute the changes in EGR to changes in the wind shear rather than N. Consequently, this indicates an increased frequency of events with increased wind shear over Svalbard and north of it manifested as positive trends in EGR (Figure 8d).

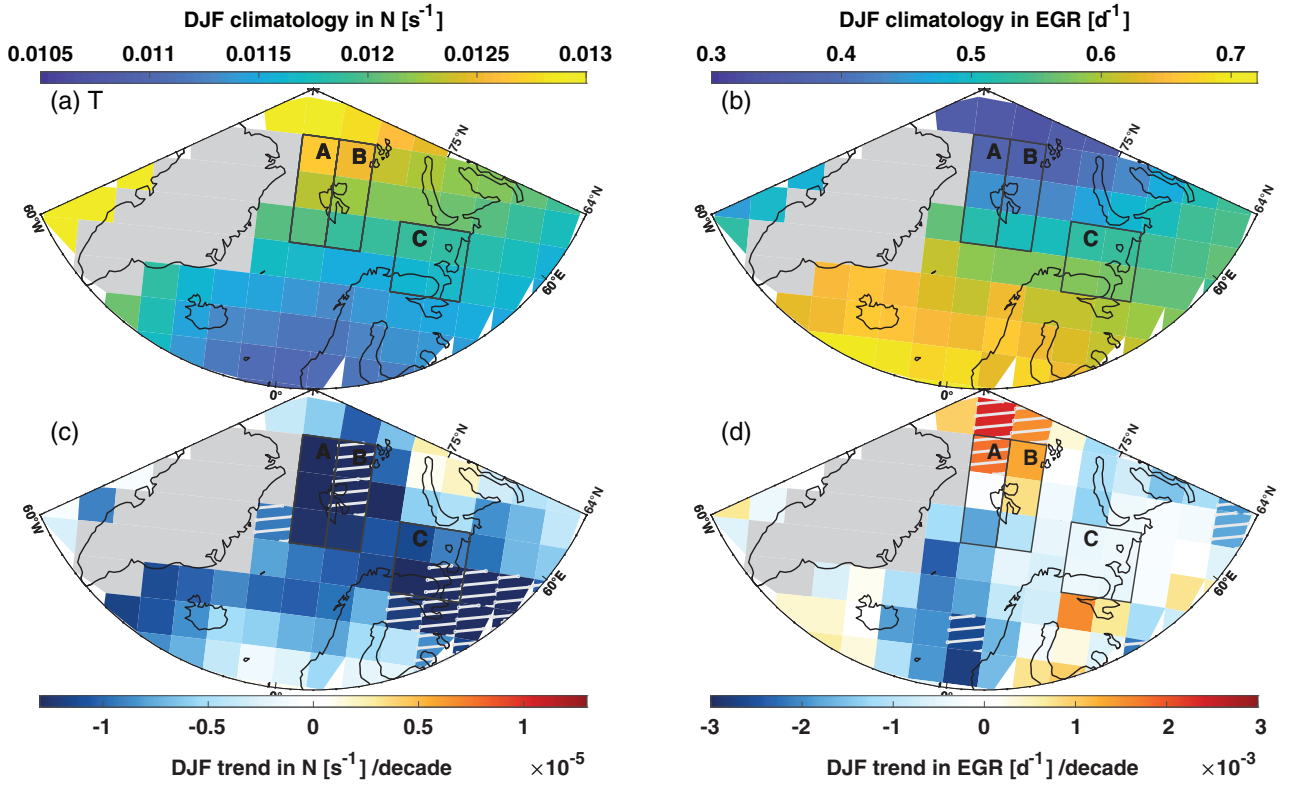

FIGURE 8 DJF climatologies of (a) static stability (N) and (b) Eady growth rate (EGR) and trends in (c) N and (d) EGR for the period 1979–2016 (see Section 2 for definitions of N and EGR). Areas where the trends are significant (90% level) are hatched. Greenland is filtered out due to high elevations

We find a positive trend in EGR over parts of and north of Svalbard and this is close to regions (Regions A and B) where we find significant positive trends in cyclone density. To the south of Svalbard, we find negative trends in EGR, but these are mostly insignificant.

Our results on baroclinicity show that there have been significant changes in both EGR and N in the vicinity of our regions of interest. These results suggest that atmospheric energetics in DJF has become more favourable for cyclone birth and development. The increased EGR and decreased N support cyclone trajectories penetrating further north, and hence, support the positive cyclone density trends found in Regions A and B.

Several previous studies have found a northward shift in the cyclone track within our study region (e.g. Tamarin-Brodsky and Kaspi, 2017). It is an intriguing question whether the observed increase in cyclone densities in Regions A and B, and the corresponding decrease in Region C, are parts of a local component of such a shift. The documented correlations between SCA and cyclone densities within these areas would support this hypothesis, and the same can be said about the increased (decreased) values of EGR (N). Furthermore, we do not find any significant temporal trends in cyclolysis or cyclogenesis (not shown) within the area of interest, which would indicate that the number of cyclones remain fairly constant over time. To shed further light on the hypothesis of a local shift in the storm track, we correlated the DJF cyclone densities in Region B and C (where the most significant changes are found). Indeed there is a significant, negative correlation between these ($R = -0.54$, p-value $= .005$).

4 | DISCUSSION AND CONCLUSIONS

In this study, we have investigated changes in cyclone activity over the high-latitude North Atlantic and their regional consequences applying a storm-tracking algorithm on ERAI 1979–2016 MSLP fields along with a composite analysis. We found the strongest significant ($p < .1$) trends in cyclone density in DJF with positive trends around Svalbard (1.3 cyclone track points per decade in Region A and 3.0 cyclone track points per decade in Region B) and negative trends in the southeastern Barents Sea (−4.5 cyclone track points per decade, Region C). A similar hotspot of DJF cyclone density increase around Svalbard and in the Barents Sea was found by Zahn *et al.* (2018) and Rudeva and Simmonds (2015). The strength of the positive trend and the exact location of this hotspot, though, vary slightly between the studies.

These discrepancies likely result from differences in the time periods analysed, the tracking algorithms used, and the geographical binning applied. However, comparing our results to those of Zahn *et al.* (2018) and Rudeva and Simmonds (2015), we can probably exclude the role of the tracking algorithms in generating differences. The tracking algorithms used in these studies are shown to produce very similar results (schemes M10 and M22 in Fig. 1 in Neu *et al.* (2013)).

However, unlike previous studies (Dong *et al.*, 2013; Rudeva and Simmonds, 2015; Tamarin-Brodsky and Kaspi, 2017; Zahn *et al.*, 2018), we also addressed the regional consequences of cyclone activity in regions showing changes over the last decades. Our study is the first to extend the scope of a cyclone density change study to local consequences in the northernmost North Atlantic. Applying composite analysis, we found cyclone activity in Regions A and B to co-occur with positive surface temperature and precipitation anomalies over Svalbard and larger parts of the Barents Sea. These manifest alongside a higher energy content of the atmospheric column, as seen by the convergence of the vertically integrated transport of dry static energy and latent heat, and a reduced net ocean surface heat loss via radiative and turbulent fluxes and a shallower Z500-Z1000 layer in the same region. The corresponding anomalies for cyclone activity in Region C are broadly similar in geographic extent, however, with opposite signs.

We found a significant negative correlation between winter cyclone densities in the northwestern (Region B) and southeastern (Region C) Barents Sea, and simultaneously no significant increase in cyclogenesis or cyclolysis in the high-latitude North Atlantic. Based on these findings, we hypothesize that a shift toward a more meridional DJF storm track in this region is responsible for the documented positive (negative) trend in cyclone density in Region B (Region C). A significant decrease in Brunt–Väisälä frequency in Region B and an increase in Eady Growth Rate north of Regions A and B support an increase in baroclinicity and, hence, enhanced cyclone activity in this region. Further, the significant correlations between SCA and cyclone densities have the best match geographically with the regions where there are significant changes in cyclone densities (Regions A, B and C). Also, SCA is the climate index with a positive (though not significant) trend over the study period, which is qualitatively in line with an increased frequency of a more meridional storm track.

Several studies have addressed the question of how climate change alters baroclinic zones and, hence, storm tracks activity (Dong *et al.*, 2013; and others). A poleward shift of the storm track is reported by a majority of these studies and, in addition, Tamarin-Brodsky and Kaspi (2017) report an enhanced poleward propagation of cyclones with the climate change. Our results with significant increases in cyclone density in the north (Regions A and B) and significant decreases the south (Region C) agree well with these results on a regional scale.

The areas in the western Barents Sea and around Svalbard, where we find significant positive trends in cyclone densities in winter (Regions A and B), have also experienced other rapid recent changes. These include the globally highest rates of wintertime 2 m air temperature increase (Førland *et al.*, 2011; Kohnemann *et al.*, 2017) and the most rapid winter sea ice decline (Parkinson and Cavalieri, 2008; Screen and Simmonds, 2010). In addition, Årthun *et al.* (2012) show that the oceanic heat inflow into the Barents Sea has increased and that this inflow controls the location of the sea ice margin in the western Barents Sea. The absence of sea ice during winter strongly alters the surface heat exchange and stratification of the air column and, hence, potentially leads to changes in cyclone intensification and dissipation (e.g. Kuo *et al.*, 1991; Jaiser *et al.*, 2012). Jaiser *et al.* (2012) further showed how the reduced stratification modulates the complex interactions of baroclinic wave energy fluxes on time-scales of a few days. Koyama *et al.* (2017) examined the possible connection between the recent Arctic sea ice loss and pan-Arctic cyclone activity. They found changes in baroclinicity suggesting an increased potential for cyclogenesis in years with low sea ice extent. Possible reasons for this could be more moisture available, regional baroclinicity, and vertical stability changes, all favouring cyclogenesis. However, when tracking individual cyclones, Koyama *et al.* (2017) did not observe a coherent increase in either cyclone frequency or intensity associated with sea ice loss.

We found cyclone activity in Regions A and B to co-occur with positive surface temperature and precipitation anomalies over Svalbard and large parts of the Barents Sea. With the large relative increase in cyclone occurrence in Regions A and B (Figure 2) and the documented increases in extreme cyclones in the region (Koyama *et al.*, 2017), there is a risk of increasing harmful (even devastating) impacts of cyclones in the Svalbard region. Especially in times with rapidly diminishing sea ice extent and rising DJF air temperatures, the additional heat and momentum from an individual cyclone might be enough to start winter melt and break-up of sea ice. Examples of high-impact wintertime cyclone events include the December 2015 storm *Frank* bringing above-zero temperatures to the North Pole (Boisvert *et al.*, 2016; Kim *et al.*, 2017; Yamagami *et al.*, 2017; Hong *et al.*, 2019). Also worth mentioning are the rain-on-snow events, such as those documented by Hansen *et al.* (2019). High-precipitation events in autumn and winter have led to destructive avalanches (Hancock *et al.*, 2018) in Svalbard.

Regional changes in cyclones, such as the increase in wintertime cyclone density over the Fram Strait found in this study, may also impact local ocean circulation. For example, Nilsen *et al.* (2016) found that an enhanced dominance of southerly wind stress, induced by the aforementioned increased cyclone densities, resulted in an increased inflow of Atlantic water into the fjords of western Spitsbergen. In turn, Luckman *et al.* (2015) found such intrusions of warm water into the fjords to be an important control of calving rates of maritime-terminating glaciers on Svalbard.

Despite reporting significant trends in cyclone occurrence for the time period 1979–2016, our results do not allow prediction of future changes in cyclones in our study region. In general, current climate models do not predict considerable intensification (deepening) of extratropical cyclones (Li *et al.*, 2014). This is, however, possibly due to challenges in modelling the factors affecting cyclone activity, which is sensitive to model resolution, atmosphere–ocean coupling, and parametrization of subgrid-scale physical processes (Willison *et al.*, 2013). Also, projected shifts in the storm tracks are a sum of several competing factors, an example being changing temperature gradients at different altitudes (Harvey *et al.*, 2014).

Focusing on the northern North Atlantic, both the historical and future changes in cyclone activity are primarily controlled by the factors affecting baroclinicity. Due to the competing effects of (a) the amplified Arctic warming, reducing the meridional temperature gradient and hence decreasing *EGR*, and (b) sea ice decline, reducing stratification and hence increasing *EGR*, the observed changes have varied between regions and also the future changes will depend on the region and time-scale addressed. Recent papers have suggested that wintertime cyclone activity in the Arctic will decrease toward the end of the century (Tamarin-Brodsky and Kaspi, 2017; Day *et al.*, 2018). However, the two competing effects on *EGR* may make the changes hard to model reliably. Further, due to sea ice loss and reduced boundary-layer stratification, near-surface winds over the northern Barents Sea and Svalbard region are in any case projected to increase (Ruosteenoja *et al.*, 2019), which, together with higher air temperatures, are expected to increase the impacts of cyclones.

AKNOWLEDGEMENTS

We acknowledge the Academy of Finland (contract 317999) for supporting Timo Vihma's contribution to this manuscript.

ORCID

S. Wickström https://orcid.org/0000-0003-3650-844X

REFERENCES

Aagaard, K. and Greisman, P. (1975) Toward new mass and heat budgets for the Arctic Ocean. *Journal of Geophysical Research*, 80(27), 3821–3827. https://doi.org/10.1029/JC080i027p03821.

Årthun, M., Eldevik, T., Smedsrud, L.H., Skagseth, Ø. and Ingvaldsen, R.B. (2012) Quantifying the influence of Atlantic heat on Barents Sea ice variability and retreat. *Journal of Climate*, 25(13), 4736–4743. https://doi.org/10.1175/jcli-d-11-00466.1.

Barnston, A.G. and Livezey, R.E. (1987) Classification, seasonality and persistence of low-frequency atmospheric circulation patterns. *Monthly Weather Review*, 115(6), 1083–1126. https://doi.org/10.1175/1520-0493(1987)115<1083:csapol>2.0.co;2.

Bengtsson, L., Hodges, K.I. and Roeckner, E. (2006) Storm tracks and climate change. *Journal of Climate*, 19(15), 3518–3543. https://doi.org/10.1175/jcli3815.1.

Boisvert, L.N., Petty, A.A. and Stroeve, J.C. (2016) The impact of the extreme winter 2015/16 Arctic cyclone on the Barents–Kara Seas. *Monthly Weather Review*, 144(11), 4279–4287. https://doi.org/10.1175/mwr-d-16-0234.1.

Bueh, C. and Nakamura, H. (2007) Scandinavian pattern and its climatic impact. *Quarterly Journal of the Royal Meteorological Society*, 133(629), 2117–2131. https://doi.org/10.1002/qj.173.

Cohen, J., Screen, J.A., Furtado, J.C., Barlow, M., Whittleston, D., Coumou, D., Francis, J., Dethloff, K., Entekhabi, D., Overland, J. and Jones, J. (2014) Recent Arctic amplification and extreme mid-latitude weather. *Nature Geoscience*, 7(9), 627–637. https://doi.org/10.1038/ngeo2234.

Cottier, F.R., Nilsen, F., Inall, M.E., Gerland, S., Tverberg, V. and Svendsen, H. (2007) Wintertime warming of an Arctic shelf in response to large-scale atmospheric circulation. *Geophysical Research Letters*, 34(10), 607–612. https://doi.org/10.1029/2007GL029948.

Day, J.J., Holland, M.M. and Hodges, K.I. (2018) Seasonal differences in the response of Arctic cyclones to climate change in CESM1. *Climate Dynamics*, 50(9–10), 3885–3903. https://doi.org/10.1007/s00382-017-3767-x.

Dee, D.P., Uppala, S.M., Simmons, A.J., Berrisford, P., Poli, P., Kobayashi, S., Andrae, U., Balmaseda, M.A., Balsamo, G., Bauer, P., Bechtold, P., Beljaars, A.C.M., van de Berg, L., Bidlot, J., Bormann, N., Delsol, C., Dragani, R., Fuentes, M., Geer, A.J., Haimberger, L., Healy, S.B., Hersbach, H., Hólm, E.V., Isaksen, L., Kållberg, P., Köhler, M., Matricardi, M., McNally, A.P., Monge-Sanz, B.M., Morcrette, J.J., Park, B.K., Peubey, C., de Rosnay, P., Tavolato, C., Thépaut, J.-N. and Vitart, F. (2011) The ERA-Interim reanalysis: configuration and performance of the data assimilation system. *Quarterly Journal of the Royal Meteorological Society*, 137(656), 553–597.

Dong, B., Sutton, R.T., Woollings, T. and Hodges, K. (2013) Variability of the North Atlantic summer storm track: mechanisms and impacts on European climate. *Environmental Research Letters*, 8(3), 034037.

Dufour, A., Zolina, O. and Gulev, S.K. (2016) Atmospheric moisture transport to the Arctic: assessment of reanalyses and analysis of transport components. *Journal of Climate*, 29(14), 5061–5081. https://doi.org/10.1175/jcli-d-15-0559.1.

Eady, E.T. (1949) Long waves and cyclone waves. *Tellus*, 1(3), 33–52. https://doi.org/10.1111/j.2153-3490.1949.tb01265.x.

Ebita, A., Kobayashi, S., Ota, Y., Moriya, M., Kumabe, R., Onogi, K., Harada, Y., Yasui, S., Miyaoka, K., Takahashi, K., Kamahori, H., Kobayashi, C., Endo, H., Soma, M., Oikawa, Y. and Ishimizu, T. (2011) The Japanese 55-year reanalysis "JRA-55": an interim report. *Scientific Online Letters on the Atmosphere*, 7, 149–152. https://doi.org/10.2151/sola.2011-038.

Førland, E.J., Benestad, R., Hanssen-Bauer, I., Haugen, J.E. and Skaugen, T.E. (2011) Temperature and precipitation development at Svalbard 1900–2100. *Advances in Meteorology*, 2011, 1–14. https://doi.org/10.1155/2011/893790.

Gelaro, R., McCarty, W., Suárez, M.J., Todling, R., Molod, A., Takacs, L., Randles, C.A., Darmenov, A., Bosilovich, M.G., Reichle, R., Wargan, K., Coy, L., Cullather, R., Draper, C., Akella, S., Buchard, V., Conaty, A., da Silva, A.M., Gu, W., Kim, G.K., Koster, R., Lucchesi, R., Merkova, D., Nielsen, J.E., Partyka, G., Pawson, S., Putman, W., Rienecker, M., Schubert, S.D., Sienkiewicz, M. and Zhao, B. (2017) The Modern-Era Retrospective analysis for Research and Applications, version 2 (MERRA-2). *Journal of Climate*, 30(14), 5419–5454. https://doi.org/10.1175/jcli-d-16-0758.1.

Hancock, H., Prokop, A., Eckerstorfer, M. and Hendrikx, J. (2018) Combining high spatial resolution snow mapping and meteorological analyses to improve forecasting of destructive avalanches in Longyearbyen, Svalbard. *Cold Regions Science and Technology*, 154, 120–132.

Hansen, B.B., Gamelon, M., Albon, S.D., Lee, A.M., Stien, A., Irvine, R.J., Sæther, B.E., Loe, L.E., Ropstad, E., Veiberg, V. and Grøtan, V. (2019) More frequent extreme climate events stabilize reindeer population dynamics. *Nature Communications*, 10(1), 1616.

Harvey, B.J., Shaffrey, L.C. and Woollings, T.J. (2014) Equator-to-pole temperature differences and the extra-tropical storm track responses of the CMIP5 climate models. *Climate Dynamics*, 43(5–6), 1171–1182. https://doi.org/10.1007/s00382-013-1883-9.

Hodges, K.I. (1995) Feature tracking on the unit sphere. *Monthly Weather Review*, 123(12), 3458–3465. https://doi.org/10.1175/1520-0493(1995)123<3458:ftotus>2.0.co;2.

Hong, J.-Y., Kim, B.-M., Baek, E.-H., Kim, J.-H., Zhang, X. and Kim, S.-J. (2019) A critical role of extreme Atlantic windstorms in Arctic warming. *Asia-Pacific Journal of Atmospheric Sciences*, 1–12. https://doi.org/10.1007/s13143-019-00123-y.

Intergovernmental Panel on Climate Change. (2013) Climate Change 2013: The Physical Science Basis. In: Stocker, T.F., Qin, D., Plattner, G.-K., Tignor, M., Allen, S.K., Boschung, J., Nauels, A., Xia, Y., Bex, V. and Midgley, P.M. (Eds.) *Contribution of Working Group I to the Fifth Assessment Report of the Intergovernmental Panel on Climate Change*. Cambridge, UK and New York, NY: Cambridge University Press, pp. 1535.

Isaksen, K., Nordli, Ø., Førland, E.J., Łupikasza, E., Eastwood, S. and Niedźwiedź, T. (2016) Recent warming on Spitsbergen – influence of atmospheric circulation and sea ice cover. *Journal of Geophysical Research: Atmospheres*, 121(20), 11913–11931. https://doi.org/10.1002/2016JD025606.

Jaiser, R., Dethloff, K., Handorf, D., Rinke, A. and Cohen, J. (2012) Impact of sea ice cover changes on the Northern Hemisphere atmospheric winter circulation. *Tellus A*, 64(1), 11595. https://doi.org/10.3402/tellusa.v64i0.11595.

Kendall, M.G. (1975) *Rank Correlation Methods*, 4th edition. London: Charles Griffin.

Kim, B.-M., Hong, J.Y., Jun, S.Y., Zhang, X., Kwon, H., Kim, S.J., Kim, J.H., Kim, S.W. and Kim, H.K. (2017) Major cause of unprecedented Arctic warming in January 2016: critical role of an Atlantic windstorm. *Scientific Reports*, 7, 40051.

Kobayashi, S., Ota, Y., Harada, Y., Ebita, A., Moriya, M., Onoda, H., Onogi, K., Kamahori, H., Kobayashi, C., Endo, H., Miyaoka, K. and Takahashi, K. (2015) The JRA-55 reanalysis: general specifications and basic characteristics. *Journal of the Meteorological Society of Japan, Series II*, 93(1), 5–48. https://doi.org/10.2151/jmsj.2015-001.

Kohnemann, S.H.E., Heinemann, G., Bromwich, D.H. and Gutjahr, O. (2017) Extreme warming in the Kara Sea and Barents Sea during the winter period 2000–16. *Journal of Climate*, 30(22), 8913–8927. https://doi.org/10.1175/jcli-d-16-0693.1.

Koyama, T., Stroeve, J., Cassano, J. and Crawford, A. (2017) Sea ice loss and Arctic cyclone activity from 1979 to 2014. *Journal of Climate*, 30(12), 4735–4754. https://doi.org/10.1175/jcli-d-16-0542.1.

Kuo, Y.-H., Shapiro, M.A. and Donall, E.G. (1991) The interaction between baroclinic and diabatic processes in a numerical simulation of a rapidly intensifying extratropical marine cyclone. *Monthly Weather Review*, 119(2), 368–384. https://doi.org/10.1175/1520-0493(1991)119<0368:tibbad>2.0.co;2.

Li, M., Woollings, T., Hodges, K. and Masato, G. (2014) Extratropical cyclones in a warmer, moister climate: a recent Atlantic analogue. *Geophysical Research Letters*, 41(23), 8594–8601. https://doi.org/10.1002/2014GL062186.

Lim, E.-P. and Simmonds, I. (2009) Effect of tropospheric temperature change on the zonal mean circulation and SH winter extratropical cyclones. *Climate Dynamics*, 33(1), 19–32. https://doi.org/10.1007/s00382-008-0444-0.

Lind, S., Ingvaldsen, R.B. and Furevik, T. (2018) Arctic warming hotspot in the northern Barents Sea linked to declining sea-ice import. *Nature Climate Change*, 8(7), 634–639. https://doi.org/10.1038/s41558-018-0205-y.

Luckman, A., Benn, D.I., Cottier, F., Bevan, S., Nilsen, F. and Inall, M. (2015) Calving rates at tidewater glaciers vary strongly with ocean temperature. *Nature Communications*, 6(1), 8566. https://doi.org/10.1038/ncomms9566.

Mann, H.B. (1945) Nonparametric tests against trend. *Econometrica: Journal of the Econometric Society*, 13(3), 245–259.

Muckenhuber, S., Nilsen, F., Korosov, A. and Sandven, S. (2016) Sea ice cover in Isfjorden and Hornsund, Svalbard (2000–2014) from remote sensing data. *The Cryosphere*, 10(1), 149–158. https://doi.org/10.5194/tc-10-149-2016.

Murray, R.J. and Simmonds, I. (1991) A numerical scheme for tracking cyclone centers from digital data. Part I: Development and operation of the scheme. *Australian Meteorological Magazine*, 39, 155–166.

Naakka, T., Nygård, T. and Vihma, T. (2018) Arctic humidity inversions: climatology and processes. *Journal of Climate*, 31, 3765–3787. https://doi.org/10.1175/JCLI-D-17-0497.1.

Naakka, T., Nygård, T., Vihma, T., Sedlar, J. and Graversen, R. (2019) Atmospheric moisture transport between mid-latitudes and the Arctic: regional, seasonal and vertical distributions. *International Journal of Climatology*, 39(6), 2862–2879. https://doi.org/10.1002/joc.5988.

Nakamura, H., Sampe, T. and Tanimoto, Y. (2013) Observed associations among storm tracks, jet streams and midlatitude oceanic

fronts. *Earth's Climate, Geophysical Monographs*, 147, 329–345. https://doi.org/10.1029/147gm18.

Neu, U., Akperov, M.G., Bellenbaum, N., Benestad, R., Blender, R., Caballero, R., Cocozza, A., Dacre, H.F., Feng, Y., Fraedrich, K., Grieger, J., Gulev, S., Hanley, J., Hewson, T., Inatsu, M., Keay, K., Kew, S.F., Kindem, I., Leckebusch, G.C., Liberato, M.L.R., Lionello, P., Mokhov, I.I., Pinto, J.G., Raible, C.C., Reale, M., Rudeva, I., Schuster, M., Simmonds, I., Sinclair, M., Sprenger, M., Tilinina, N.D., Trigo, I.F., Ulbrich, S., Ulbrich, U., Wang, X.L. and Wernli, H. (2013) IMILAST: a community effort to intercompare extratropical cyclone detection and tracking algorithms. *Bulletin of the American Meteorological Society*, 94, 529–547. https://doi.org/10.1175/BAMS-D-11-00154.1.

Nilsen, F., Cottier, F., Skogseth, R. and Mattsson, S. (2008) Fjord–shelf exchanges controlled by ice and brine production: the interannual variation of Atlantic water in Isfjorden, Svalbard. *Continental Shelf Research*, 28(14), 1838–1853. https://doi.org/10.1016/j.csr.2008.04.015.

Nilsen, F., Skogseth, R., Vaardal-Lunde, J. and Inall, M. (2016) A simple shelf circulation model: intrusion of Atlantic water on the West Spitsbergen Shelf. *Journal of Physical Oceanography*, 46(4), 1209–1230. https://doi.org/10.1175/jpo-d-15-0058.1.

Onarheim, I.H. and Årthun, M. (2017) Toward an ice-free Barents Sea. *Geophysical Research Letters*, 44(16), 8387–8395. https://doi.org/10.1002/2017GL074304.

Onarheim, I.H., Eldevik, T., Årthun, M., Ingvaldsen, R.B. and Smedsrud, L.H. (2015) Skillful prediction of Barents Sea ice cover. *Geophysical Research Letters*, 42(13), 5364–5371. https://doi.org/10.1002/2015GL064359.

Parkinson, C.L. and Cavalieri, D.J. (2008) Arctic sea ice variability and trends, 1979–2006. *Journal of Geophysical Research*, 113(C7), 1–28. https://doi.org/10.1029/2007JC004558.

Petterssen, S. (1957) Weather observations, analysis, and forecasting. *Meteorological Research Reviews, Meteorological Monographs*, 3, 114–151. https://doi.org/10.1007/978-1-940033-25-9_1.

Rinke, A., Maturilli, M., Graham, R.M., Matthes, H., Handorf, D., Cohen, L., Hudson, S.R. and Moore, J.C. (2017) Extreme cyclone events in the Arctic: wintertime variability and trends. *Environmental Research Letters*, 12(9), 094006. https://doi.org/10.1088/1748-9326/aa7def.

Rudeva, I. and Simmonds, I. (2015) Variability and trends of global atmospheric frontal activity and links with large-scale modes of variability. *Journal of Climate*, 28(8), 3311–3330. https://doi.org/10.1175/jcli-d-14-00458.1.

Ruosteenoja, K., Vihma, T. and Venäläinen, A. (2019) Projected changes in European and North Atlantic seasonal wind climate derived from CMIP5 simulations. *Journal of Climate*, 32(19), 6467–6490.

Saha, S., Nadiga, S., Thiaw, C., Wang, J., Wang, W., Zhang, Q., van den Dool, H.M., Pan, H.L., Moorthi, S., Behringer, D., Stokes, D., Peña, M., Lord, S., White, G., Ebisuzaki, W., Peng, P. and Xie, P. (2006) The NCEP climate forecast system. *Journal of Climate*, 19(15), 3483–3517. https://doi.org/10.1175/jcli3812.1.

Screen, J.A., Bracegirdle, T.J. and Simmonds, I. (2018) Polar climate change as manifest in atmospheric circulation. *Current Climate Change Reports*, 4(4), 383–395.

Screen, J.A. and Simmonds, I. (2010) The central role of diminishing sea ice in recent Arctic temperature amplification. *Nature*, 464(7293), 1334–1337.

Sen, P.K. (1968) Estimates of the regression coefficient based on Kendall's tau. *Journal of the American Statistical Association*, 63(324), 1379–1389.

Sepp, M. and Jaagus, J. (2011) Changes in the activity and tracks of Arctic cyclones. *Climatic Change*, 105(3–4), 577–595. https://doi.org/10.1007/s10584-010-9893-7.

Serreze, M.C. (1995) Climatological aspects of cyclone development and decay in the Arctic. *Atmosphere–Ocean*, 33(1), 1–23. https://doi.org/10.1080/07055900.1995.9649522.

Serreze, M.C. and Barrett, A.P. (2008) The summer cyclone maximum over the central Arctic Ocean. *Journal of Climate*, 21(5), 1048–1065. https://doi.org/10.1175/2007jcli1810.1.

Serreze, M.C., Box, J.E., Barry, R.G. and Walsh, J.E. (1993) Characteristics of Arctic synoptic activity, 1952–1989. *Meteorology and Atmospheric Physics*, 51(3–4), 147–164. https://doi.org/10.1007/bf01030491.

Shepherd, T.G. (2014) Atmospheric circulation as a source of uncertainty in climate change projections. *Nature Geoscience*, 7(10), 703–708. https://doi.org/10.1038/ngeo2253.

Simmonds, I., Burke, C. and Keay, K. (2008) Arctic climate change as manifest in cyclone behavior. *Journal of Climate*, 21(22), 5777–5796. https://doi.org/10.1175/2008jcli2366.1.

Simmonds, I. and Lim, E.-P. (2009) Biases in the calculation of Southern Hemisphere mean baroclinic eddy growth rate. *Geophysical Research Letters*, 36(1), 115. https://doi.org/10.1029/2008GL036320.

Simmonds, I. and Rudeva, I. (2014) A comparison of tracking methods for extreme cyclones in the Arctic basin. *Tellus A*, 66(1), 25252.

Smedsrud, L.H., Ingvaldsen, R.B., Nilsen, J.E.Ø. and Skagseth, Ø. (2010) Heat in the Barents Sea: transport, storage, and surface fluxes. *Ocean Science*, 6(1), 219–234. https://doi.org/10.5194/os-6-219-2010.

Sorteberg, A. and Walsh, J.E. (2008) Seasonal cyclone variability at 70°N and its impact on moisture transport into the Arctic. *Tellus A*, 60(3), 570–586. https://doi.org/10.3402/tellusa.v60i3.15372.

Tamarin-Brodsky, T. and Kaspi, Y. (2017) Enhanced poleward propagation of storms under climate change. *Nature Geoscience*, 10(12), 908–913. https://doi.org/10.1038/s41561-017-0001-8.

Theil, H. (1949) *A Rank-invariant Method of Linear and Polynomial Regression Analysis, 1-2; Confidence Regions for the Parameters of Linear Regression Equations in Two, Three and More Variables: (proceedings Knaw, _5_3(1950), Nr 3/4, Indagationes Mathematicae, _1_2(1950), P 85-91, P 173-177)*.

Tsukernik, M., Kindig, D.N. and Serreze, M.C. (2007) Characteristics of winter cyclone activity in the northern North Atlantic: insights from observations and regional modeling. *Journal of Geophysical Research*, 112(D3), 1–19. https://doi.org/10.1029/2006JD007184.

Vihma, T., Graversen, R., Chen, L., Handorf, D., Skific, N., Francis, J.A., Tyrrell, N., Hall, R., Hanna, E., Uotila, P., Dethloff, K., Karpechko, A.Y., Björnsson, H. and Overland, J.E. (2019) Effects of the tropospheric large-scale circulation on European winter temperatures during the period of amplified Arctic warming. Accepted for publication in. *International Journal of Climatology*, 1–21. https://doi.org/10.1002/joc.6225.

Vihma, T. and Pirazzini, R. (2005) On the factors controlling the snow surface and 2-m air temperatures over the Arctic Sea ice in winter. *Boundary-Layer Meteorology*, 117(1), 73–90. https://doi.org/10.1007/s10546-004-5938-7.

Vihma, T., Screen, J., Tjernström, M., Newton, B., Zhang, X., Popova, V., Deser, C., Holland, M. and Prowse, T. (2016) The atmospheric role in the Arctic water cycle: a review on processes, past and future changes, and their impacts. *Journal of Geophysical Research: Biogeosciences*, 121(3), 586–620. https://doi.org/10.1002/2015JG003132.

Wallace, J.M. and Hobbs, P.V. (2006) Introduction and overview. *In Atmospheric Science*, 2nd Edition, 1–23. New York, NY: Academic Press. https://doi.org/10.1016/b978-0-12-732951-2.50006-5.

Willison, J., Robinson, W.A. and Lackmann, G.M. (2013) The importance of resolving mesoscale latent heating in the North Atlantic storm track. *Journal of the Atmospheric Sciences*, 70(7), 2234–2250. https://doi.org/10.1175/jas-d-12-0226.1.

Yamagami, A., Matsueda, M. and Tanaka, H.L. (2017) Extreme Arctic cyclone in August 2016. *Atmospheric Science Letters*, 18(7), 307–314. https://doi.org/10.1002/asl.757.

Yilmaz, A.G. and Perera, B.J.C. (2015) Spatiotemporal trend analysis of extreme rainfall events in Victoria, Australia. *Water Resources Management*, 29, 4465–4480.

Zahn, M., Akperov, M., Rinke, A., Feser, F. and Mokhov, I.I. (2018) Trends of cyclone characteristics in the Arctic and their patterns from different reanalysis data. *Journal of Geophysical Research: Atmospheres*, 123(5), 2737–2751. https://doi.org/10.1002/2017JD027439.

Zhang, X., Walsh, J., Zhang, J., Bhatt, U.S. and Ikeda, M. (2004) Climatology and interannual variability of Arctic cyclone activity: 1948–2002. *Journal of Climate*, 17(12), 2300–2317. https://doi.org/10.1175/1520-0442(2004)017<2300:caivoa>2.0.co;2.

How to cite this article: Wickström S, Jonassen MO, Vihma T, Uotila P. Trends in cyclones in the high-latitude North Atlantic during 1979–2016. *Q J R Meteorol Soc*. 2020;146:762–779. https://doi.org/10.1002/qj.3707